Tropical and global scale interactions among water vapor, atmospheric greenhouse effect, and surface temperature

Anand K. Inamdar and V. Ramanathan

Center for Clouds, Chemistry and Climate, Center for Atmospheric Sciences, Scripps Institution of Oceanography, University of California, San Diego

Abstract. We employ a multitude of global data sets to extend recent analyses of atmospheric greenhouse effect and its dependence on surface temperature (T_S) and vertical water vapor distribution. The new data encompasses a global domain including both the continents and the oceans as well as both the ascending and descending branches of the Walker and Hadley cells and the extratropical storm track regions. We adopt the radiometric definition of the atmospheric greenhouse effect, G_a, which is the difference between the surface longwave emission and the outgoing longwave radiation. We derive the global average greenhouse effect over both oceans and land areas. The east to west variations of the normalized atmospheric greenhouse effect (g_a) and precipitable water (w) are just as strong as the north to south variations, thus illustrating the strong role of the dynamics in w and g_a. Between 60°N and 60°S the lowest values of g_a (0.11–0.15) are found over the Saharan and other deserts; while the largest values (0.35–0.40) are found over the warm oceans with a deep convective atmosphere. The coupling between G_a, and the vertical distribution of atmospheric water vapor and temperature, is examined from monthly mean annual cycle. When averaged from the southern to the northern latitudes, these quantities exhibit a statistically significant annual cycle. The annual cycle of T_S, about 1 K for the tropics (30°N to 30°S) and about 4 K for the globe, is large enough to obtain a statistically significant estimate for the sensitivity parameter dG_a/dT_S. It is as large as 5.5–6 W m^{-2} K^{-1} for tropical mean conditions (30°N to 30°S) and reduces to a global mean value of 3.5 W m^{-2} K^{-1} (with a 2σ range of 2.9–4.1 W m^{-2} K^{-1}). Consistent with earlier studies, the tropics exhibit a strong positive coupling between T_S, G_a, and water vapor distribution with large increases in the midtroposphere humidity. However, poleward of 30°N, water vapor increases are about half as much as that in the tropics, and the sensitivity parameter dG_a/dT_S decreases. This is because poleward of 30°, the annual cycle is dominated by land surface temperature changes which are not so effective as sea surface temperature changes in enhancing the water vapor greenhouse effect. Irrespective of the region (ocean or land) or the latitude domain (tropics or extratropics), the data presented here do not offer any support for the suggestion that increases in tropical or global mean surface temperature would lead to a decrease in water vapor greenhouse effect by drying the middle to upper troposphere. If any, the global scale sensitivity derived from the annual cycle is consistent with the magnitude of the positive feedback obtained by general circulation models.

1. Introduction

Water vapor feedback forms one of the greatest uncertainties in projecting future climate changes. A simple picture of the operation of water vapor feedback can be given as follows: An increase in the atmospheric CO_2 and other greenhouse gases causes the surface and the troposphere to warm. Associated with this warming is an increase in atmospheric water vapor content (due to the temperature dependence of the saturation vapor pressure) which further enhances the warming through the water vapor greenhouse effect. Such a positive water vapor feedback was included in the pioneering works of *Arrhenius* [1896] and *Manabe and Wetherald* [1967].

The empirical evidence used to model the water vapor feedback [*Arrhenius*, 1896; *Manabe and Wetherald*, 1967] is the

observed fact that the tropospheric relative humidity at most latitudes remains roughly the same between winter and summer inspite of the significant variations in temperatures. As a result of this fixed relative humidity assumption, when the surface and troposphere warm (say due to increase in CO_2), moisture levels in the atmosphere undergo enhancement. The fundamental reason for the latitudinal and seasonal invariance of the tropospheric relative humidity has not been explained yet; however, atmospheric dynamics must play a fundamental role in regulating the relative humidity [also see *Bengtsson*, 1997].

Several general circulation models [*Cess et al.*, 1990; *IPCC*, 1995] simulate this positive feedback, inspite of employing widely varying parameterization schemes for deep convection. The deep convection is relevant in this context, because it plays an important role in the water vapor transport [*Lindzen*, 1990]. It has already been shown [*Inamdar and Ramanathan*, 1994; *Soden et al.*, 1995] that deep convection increases the middle to upper tropospheric moisture on regional scales. *Cess* [1991]

and *Rind et al.* [1991] argued in favor of the positive feedback based on strong supporting evidence from both model and observations. *Raval and Ramanathan* [1989] (hereinafter referred to as RR) attempted to quantify the interactions among the sea surface temperature, greenhouse effect, and water vapor distribution employing data from the Earth Radiation Budget Experiment (ERBE). By formulating the atmospheric greenhouse effect as the difference between the surface and the top-of-atmosphere (TOA) emissions of the longwave radiative energy, they were able to get an "observable" estimate of the atmospheric greenhouse effect and estimated dG_a/dT_S from regional variations in G_a and T_S. As shown by *Dutton* [1995], G_a and dG_a/dT_S enter directly into the governing equations for climate change.

Subsequent studies [*Lindzen*, 1994; *Lindzen et al.*, 1995; *Bony et al.*, 1995; *Lau et al.*, 1996], however, have held the view that the observed changes [*Rind et al.*, 1991; RR] are domain specific, being strongly influenced by the circulation patterns elsewhere, and hence do not constitute a true estimate of the feedback effect. Their argument was that mutually compensative mechanisms were at work on a global level and these have been ignored in the earlier studies. Thus there is a need to reevaluate the RR feedback analysis which would account for these mutually compensative phenomena on a global scale. The obvious way to settle the issue is to compare the decadal and long-term variation in temperature and moisture. Studies that have attempted this [*Hense et al.*, 1988; *Flohn et al.*, 1989] have shown that trends in humidity and temperature are positively correlated, supporting positive water vapor feedback. However, instrumental and sampling uncertainties [*Gaffen et al.*, 1991] limit the accuracy of the observed trends. In this study we avoid these experimental errors by focusing on the annual cycle, employing a 2–5 year period of new global data sets that are available.

A main objective of the present study is to address these specific issues by extending the analysis of *Raval and Ramanathan* [1989] in geography and time and encompassing both land and oceans. In this study we use the annual cycle of tropical (30°N to 30°S), global (90°N–90°S) means, and global mean surface temperatures to provide yet another test of the water vapor feedback. As pointed out by *Lindzen et al.* [1995], this annual cycle of surface and atmospheric temperature changes on tropical and global mean scales provide a critical test of the performance of climate models. We will be using a multitude of data sets from several different sources in our analysis. We are not aware of a similar study that combines the land surfaces and oceans together. The present work represents the first such effort to include both ocean and land surfaces in the analysis of the greenhouse effect and thus attempt to get a better understanding of the global water vapor feedback issue.

2. Data Sources

The TOA outgoing longwave fluxes have been retrieved from the Earth Radiation Budget Experiment (ERBE) scanner data aboard the NOAA satellite [*Barkstrom*, 1984]. These are monthly means covering the period 1985–1989 on a global 2.5° (latitude) × 2.5° (longitude) grid [*Barkstrom et al.*, 1989]. We are considering only the open oceans and land surface and ignore the sea ice and permanent ice regions, for lack of reliability of the data over the ice-covered surfaces. The latter account for about 6% of the planet's surface.

Three sources have been used here for the surface temperature. Over the ice-free oceans, *Reynolds* [1988] blended analyses of data collected from ships, buoys, and satellites have been employed. An equivalent data set is not available for the land surface, so we use the ground temperatures extracted from the interdisciplinary data collection series of the Data Assimilation Office, which has produced version 1 [*Schubert et al.*, 1993] of the Goddard Earth Observing System Data Assimilation System (DAO GEOS-1). These are a synthesis of observations consisting of globally deployed in situ and remote measurements and short-term model forecasts. DAO multi-year assimilation products have been validated by comparing with other analysis products such as ECMWF and have been considered well suited for climate research [*Schubert et al.*, 1995]. The subset of monthly means, which we use here, extracted from the full 3 hourly time series has been regridded into a 2.5 × 2.5° grid to conform to the ERBE data scale. However, there have been reports of a cold bias in the data set, as we shall show soon in the section, and so we use an additional source to examine the severity of this problem. The other source of these data comes from the National Meteorological Center (NMC) surface temperature data archive at the National Center for Atmospheric Research (NCAR). These constitute the surface observations at individual stations on a 6 hourly basis over the globe. These also have been converted into a monthly 2.5 × 2.5° grid means for the years 1988 and 1989.

The precipitable water content in the atmosphere over the oceans is retrieved from the Special Sensor Microwave Imager (SSM/I) data aboard the DMSP-F8 satellite. These data are available as a monthly mean converted to a 2.5 × 2.5° grid from July 1987, thus providing an overlap of a little over 2 years with the ERBE. Again SSM/I is not available over the land surfaces. Recently, there has been an effort [*Randel et al.*, 1996] to produce a global moisture data set as part of the GEWEX (Global Energy and Water Cycle Experiment) program. *Randel et al.* [1996] have produced a 5 year total and layered global water vapor data set by synthesizing radiosonde observations, Television and Infrared Operational Satellite Operational Vertical Sounder (TOVS), and SSM/I measurements. This data set is referred to as the NASA water vapor project (NVAP) [*Randel et al.*, 1996].

2.1. Data Compatibility

Because of the independent sources for the surface temperature and precipitable water, a compatibility test was performed. Both the GEOS-1-derived ground surface temperatures and the NVAP precipitable water data have global coverage, while the Reynolds NMC-blended analysis and SSM/I are available only over the ice-free ocean regions. The ocean surface temperatures have been prescribed in the GEOS assimilations. The NMC station data have been retrieved only for the land surfaces. For precipitable water vapor, the SSM/I measurements are considered to be more accurate than the TOVS retrievals. Accordingly, a higher weight has been assigned to the SSM/I measurements [*Randel et al.*, 1996] in the derivation of the NVAP water vapor data product and further elaborate quality checks have been performed keeping in mind the limitations of different data sets. Nevertheless, since we will be using a mix of these data sets, it is found prudent to compare them for compatibility wherever possible.

Table 1 presents a summary of the comparisons for both temperature and precipitable water for the years 1988 and

Table 1. Mean, Difference, and Standard Deviation Between GEOS-1 Surface Temperatures and Those Retrieved From NMC Surface Data Records for 1988 and 1989 and between the Precipitable Water Derived From the SSM/I Instrument and the NVAP Water Vapor Data

Parameter Description	1988, K	1989, K
Surface Temperature		
T_S from GEOS-1	mean, 284.3	mean, 284.3
T_S from NMC surface observations	mean, 287.1	mean, 287.2
GEOS-1 and NMC surface observations	mean, −2.8 s.d., 4.4	mean, −2.8 s.d., 4.4

Parameter Description	1988, g cm^{-2}	1989, g cm^{-2}
Total Precipitable Water Vapor		
SSM/I	mean, 2.5985	mean, 2.5427
NVAP	mean, 2.6141	mean, 2.5439
|SSM/I − NVAP|	mean, 0.1715 s.d., 0.158	mean, 0.1496 s.d., 0.144

1989. Because of the nature of the data sets and their sources we are limited to perform only partial comparisons. For the surface temperature we compare the GEOS with station data. Table 1 entries show the annual global averages for the years 1988 and 1989 for both the surface temperature and the total precipitable water. It is apparent that the GEOS-1 temperatures have a distinct cold bias by about 3 K compared to the station data on a global annual basis. Further, resolving this into seasonal estimates shows the bulk of the bias occurs during the winter months, as revealed by the histograms of temperature differences shown in Figure 1 for January and July 1989. However, one should also bear in mind the sampling issue and the instrument differences at different places for the station data. However, there is a reasonable agreement for the water vapor data, which may be partly due to the higher weight assigned to the SSM/I over the oceans which cover about two thirds of the Earth.

To estimate the greenhouse effect over the continent regions, we need, in addition, the surface emissivities, because land surfaces do not necessarily emit as black bodies. A spectrally dependent detailed emissivity data for different seasons over the globe is not available at the present time. However, a broadband and window component of surface emissivities has been compiled by D. Kratz et al. (personal communication, 1996) based on the *Salisbury et al.* [1992] emissivity values in the 8–14 μm atmospheric window. These data have been used in computing the greenhouse effect over land surfaces.

3. Relation Among OLR, G_a, and the Feedback Parameters

Consider first a one-dimensional system with the surface emitting like a blackbody. The clear-sky outgoing longwave radiation (F_C) and G_a are related by

$$F_C = \sigma T_S^4 - G_a \qquad (1)$$

where T_S is the surface temperature and G_a, by definition, is given by

$$G_a = \int_{\infty}^{0} dz' \int_{4\,\mu m}^{500\,\mu m} [1 - e^{-\tau_v(z',\infty)}] \frac{dB_v(z')}{dz'} dv \qquad (2)$$
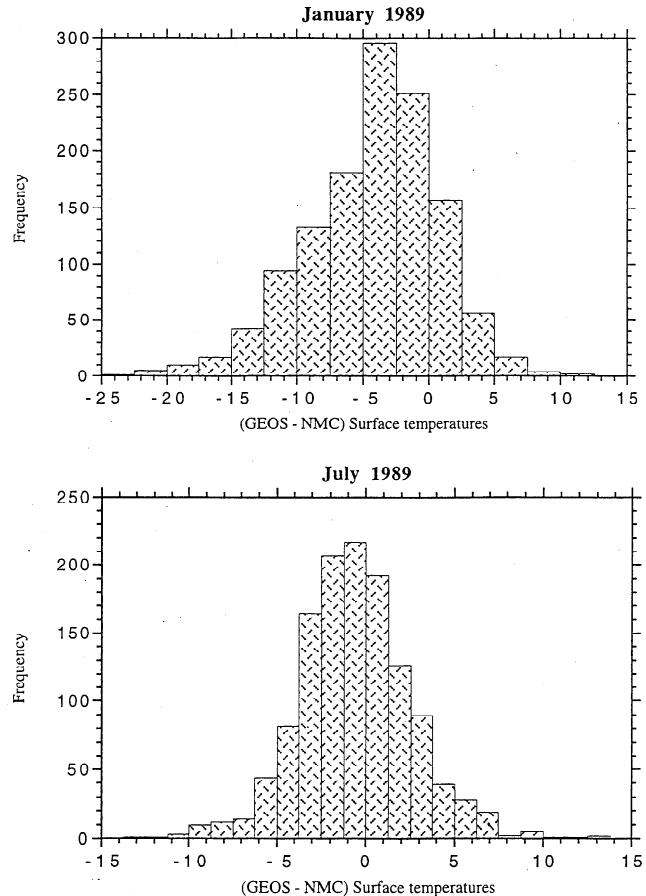

Figure 1. Histogram or frequency distribution of temperature differences (GEOS 1, NMC surface station data) for the months of January and July 1989. The top panel of the figure highlights the cold bias of the GEOS data set.

where τ_v represents the optical depth between TOA and z' and the expression in square parenthesis thus represents the absorptance. From (1) we note that G_a is the reduction in the outgoing longwave radiation due to the presence of the atmosphere. From (2) it is seen that the reduction in OLR depends on two factors: τ_v, the optical depth, and the vertical temperature gradient (note that $dB_v/dz \equiv dB_v/dT^*dT/dz$). Without a radiatively active atmosphere, i.e., $\tau_v = 0$, $G_a = 0.0$ and OLR would be identically equal to σT_S^4. Likewise, without a vertical temperature gradient, $dB_v/dz = 0$, and $G_a = 0$. It is obvious that G_a includes the contribution from the entire troposphere and the stratosphere with equal weight given to all regions.

The greenhouse effect of the atmosphere and clouds (G) is obtained from

$$F = \sigma T_S^4 - G \qquad (3)$$

where F is the OLR for the average cloudy skies. Note that $G = G_a + C_{lw}$, where C_{lw}, the longwave cloud forcing [*Ramanathan et al.*, 1989] denotes the enhancement of the greenhouse effect by clouds. The fundamental longwave climate feedback parameter is dF/dT_S, and from (3),

$$dF/dT_S = 4\sigma T_S^3 - dG/dT_S = 4\sigma T_S^3 - (dG_a/dT_S$$
$$+ dC_{lw}/dT_S) \qquad (4)$$

Table 2. Global Longwave Radiative Energy Budget Components (W m^{-2}) Derived Using Different Sources for Land Surface Temperatures

	Ocean Surface Temperatures: NMC-Blended Analysis [Reynolds, 1988] Land Surface Temperatures (As Below)								
	GEOS (1985–1989)			GEOS (1988–1989)			NMC Station Data (1988–1989)		
Parameter	Ocean	Land	Ocean Plus Land	Ocean	Land	Ocean Plus Land	Ocean	Land	Ocean Plus Land
$\langle T_S \rangle$	292.9	285.2	290.7	293.2	285.4	291.0	293.2	288.0	292.1
$\langle E_S \rangle$[a]	419.8	380.8	408.8	421.0	381.5	409.9	421.0	392.9	414.9
$\langle F_C \rangle$	274.7	265.2	272.0	275.6	265.4	272.8	275.6	265.7	273.5
$\langle G_a \rangle$	145.2	115.6	136.9	145.4	116.1	137.2	145.4	127.2	141.4

[a]For ocean surfaces, $E_S = \varepsilon \sigma T_S^4$; over nonblack surfaces it is modified to account for reflection of atmospheric emission to the surface (assumed as 80% of the surface blackbody emission), $E_S = \varepsilon \sigma T_S^4 + (1 - \varepsilon)*0.8*\sigma T_S^4$.

The water vapor feedback effect is contained in dG_a/dT_S; the cloud feedback effect is contained in dC_{lw}/dT_S, and lapse rate changes will influence both dG_a/dT_S and dC_{lw}/dT_S. Considering first dG_a/dT_S, we obtain from (1)

$$dG_a/dT_S = 4\sigma T_S^3 - dF_C/dT_S \qquad (5)$$

For a uniform change in surface and atmospheric temperature (i.e., without lapse rate feedback) and without any change in water vapor amount (i.e., no water vapor feedback), $dF_C/dT_S \approx 3.3$ W m^{-2} K^{-1} [Ramanathan, 1981]. Thus for lapse rate or water vapor to exert a positive feedback requires

$$dF_C/dT_S < 3.3 \text{ W m}^{-2} \text{ K}^{-1} \quad \text{for positive feedback}$$
$$\approx 3.3 \text{ W m}^{-2} \text{ K}^{-1} \quad \text{for no feedback}$$
$$\geq 3.3 \text{ W m}^{-2} \text{ K}^{-1} \quad \text{for negative feedback}$$
$$(6)$$

One-dimensional radiative-convective models with fixed relative humidity assumption yield [see Ramanathan, 1981]

$$dF_C/dT_S \approx 2 \text{ W m}^{-2} \text{ K}^{-1} \qquad (7)$$

To rephrase the above criteria in terms of (equation (5)), we note that for global average, $T_S = 289$ K, $4\sigma T_S^3 = 5.47$ W m^{-2} K^{-1}, and we obtain from (5) and (6)

$$dG_a/dT_S > 2.2 \text{ W m}^{-2} \text{ K}^{-1} \quad \text{for positive feedback}$$
$$\approx 2.2 \text{ W m}^{-2} \text{ K}^{-1} \quad \text{for no feedback}$$
$$< 2.2 \text{ W m}^{-2} \text{ K}^{-1} \quad \text{for negative feedback}$$
$$(8)$$

Caveat on (5): If we relax the assumption of a one-dimensional system, we have to account for two complicating factors.

1. For a regionally varying surface temperature (as opposed to the one-dimensional system considered above), (1) should be replaced by

$$F_C = \sigma \langle T_S^4 \rangle - G_a \qquad (9)$$

where the angle brackets indicate space and time averages. We can easily show that $\langle T_S^4 \rangle$ is greater than $\langle T_S \rangle^4$.

$$dG_a/dT_S = \sigma d\langle T_S^4 \rangle/dT_S - dF_C/dT_S$$

In general, $\sigma d\langle T_S^4 \rangle/dT_S \neq 4\sigma \langle T_S \rangle^3$. In this paper we adopt the following procedure: For estimates of average G_a values shown in Table 2 (Figures 2a and 2b, and Plate 1) we adopt the correct averaging procedure as shown in (9). However, to es-

timate the feedback parameter dG_a/dT_S, we adopt the simplified expression given by (5). This is because earlier studies report only dF_C/dT_S and the average T_S, and to convert their OLR feedback into dG_a/dT_S, we have to resort to (5).

2. The second factor concerns nonblackbody emission. Sea surface is within 1% of emitting like a blackbody, and hence the upflux at the surface estimated by assuming a blackbody emission is within few tenths of a percent (≈ 0.2–0.4%) of the correct value. Land surfaces, however, can deviate substantially from blackbody emission. Emissivity of deserts can be as low as 0.85. For nonblack surfaces we modify the surface emission (E_S) as follows:

$$E_S = \varepsilon \sigma T_S^4 + (1 - \varepsilon) F^-$$

where ε is the surface emissivity and F^- is the downward longwave flux at the surface. In the tropics, F^- is about 90–
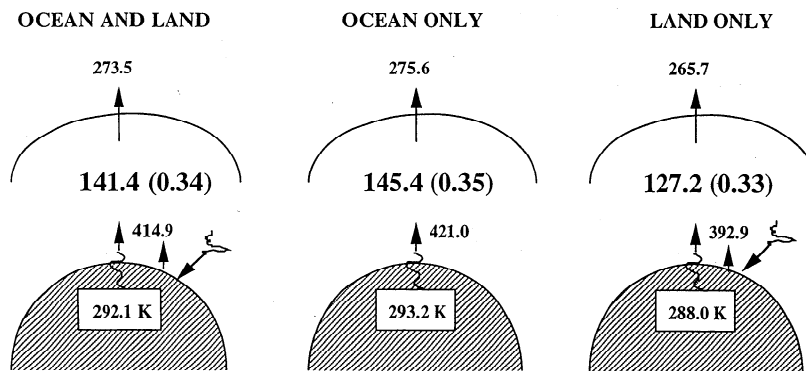
GLOBAL AVERAGE ATMOSPHERIC GREENHOUSE EFFECT (W m^{-2})

267.5

131.1 (0.334)

398.6

288.35 K
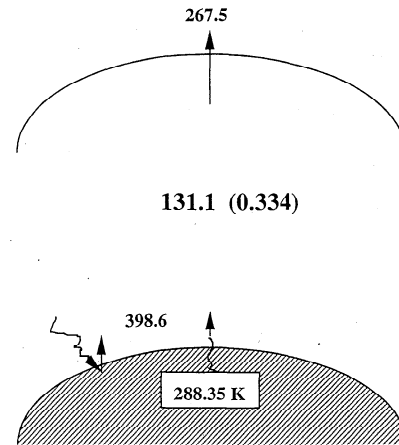
Includes sea ice and permanent ice regions.

Uncertainties:
surface emission: ± 3 W m^{-2}
TOA flux: ± 5 W m^{-2}
G_a: ± 6 W m^{-2}

Figure 2a. Global average of surface temperature, surface emission, outgoing longwave radiation (OLR), and atmospheric greenhouse effect derived from ERBE, GEOS data (1985–1989), and Salisbury et al. [1992] surface emissivity tables. The results include all regions of the globe including sea ice and permanent ice.

GLOBAL AVERAGE ATMOSPHERIC GREENHOUSE EFFECT (W m^{-2})

Figure 2b. Global average of surface temperature, surface emission, outgoing longwave radiation, and atmospheric greenhouse effect derived from ERBE, NMC-blended sea surface temperature (SST) (for the oceans), NMC station surface temperatures (for the land), and *Salisbury et al.* [1992] surface emissivity tables for the period 1988–1989. Results exclude the ice-covered regions.

95% of σT_S^4, while for global average conditions, it is about 80%. Thus the net effect of nonblack emissivity is much smaller than that indicated by the value of ε. Instead of estimating F^-, at each grid point, we let $F^- = 0.8\,\sigma T_S^4$. The error introduced by this assumption on G_a is much less than a percent.

4. Global Averages

Unless otherwise mentioned, results shown here and elsewhere use station data for land surface temperatures which are restricted to a 2 year period from 1988 to 1989. However, using the GEOS data, we compare 2 year averages with 5 year averages (1985 to 1989) to assess the importance of interannual variations. As shown later, for the large-scale average results (tropical and global) the 2 year averages are virtually identical to 5 year averages.

The area averages were obtained as follows: Each grid point value is first weighted by its area, and all of the area-weighted values within the specified domain (tropical or global and ocean or ocean plus land) for each month were then summed and, subsequently, normalized by the domain area (be it tropical or global) to obtain the monthly domain average value. Another method (not followed here) is to obtain zonal averages first and then weight the zonal mean with the area of the particular latitude zone. The two methods yield significantly different averages, particularly when we consider just oceanic regions (as opposed to ocean plus land). Furthermore, unless otherwise mentioned, we do not include sea ice and land ice (e.g., Greenland and Antarctic) points in any of our averages.

The global annual means for the surface temperature and the different radiative flux parameters extracted from the ERBE are shown in Figures 2a and 2b. The ERBE clear-sky classification scheme is known to be inefficient over the ice-covered surfaces. Hence all the results in this study, with the exception of Figure 2a, excludes the ice-covered Earth. Yet it

would be of interest to know the globally averaged radiation budget which includes all regions of the Earth. Thus we present in Fig. 2a the radiation budget for the entire planet using GEOS data (1985–1989). The ice-covered portion of the Earth constitutes ~6% of the globe. Table 2 shows the effect of using different averaging periods and also different sources of land surface temperatures. The 2 year GEOS results are almost identical to the 5 year averages. The numbers for the land and the land/ocean composite are systematically lower for the GEOS data due to the ground temperature bias discussed in section 3. Also, it is apparent from Figure 2b and Table 2 that the global surface temperatures have a warmer bias of about 4 K due to the exclusion of ice surfaces.

In addition to the exclusion of ice-covered surface in the analysis, it was further discovered that the clear-sky ERBE OLR data were missing in about 8% of the ocean and 10% of the land regions. Thus the global averages depicted in Figure 2b exclude sea ice (3%), permanent ice (3%), and regions masked by missing ERBE data (~8%). When regions with the missing ERBE data mask were included, the corresponding global annual mean surface temperatures for the oceans, land, and composite turn out to be 292.4, 284.3, and 290 K, respectively. Upon comparing these numbers with the temperatures in Figure 2b, we infer that the missing ERBE data correspond mostly to regions of lower surface temperatures, further contributing to the warm bias in global-average surface temperature.

The regional distribution of the key parameters for the globe (60°N–60°S) is shown in Plate 1. The top panel of Plate 1 shows the annual mean distribution of the normalized greenhouse effect $g_a = G_a/\sigma T_S^4$. A large fraction of the spatial variation in G_a is due to variations in T_S. The contributions from variations in T_S are essentially removed in the normalized greenhouse effect (g_a), such that regional variations of g_a (shown in the top panel of Plate 1) reveal the effects of
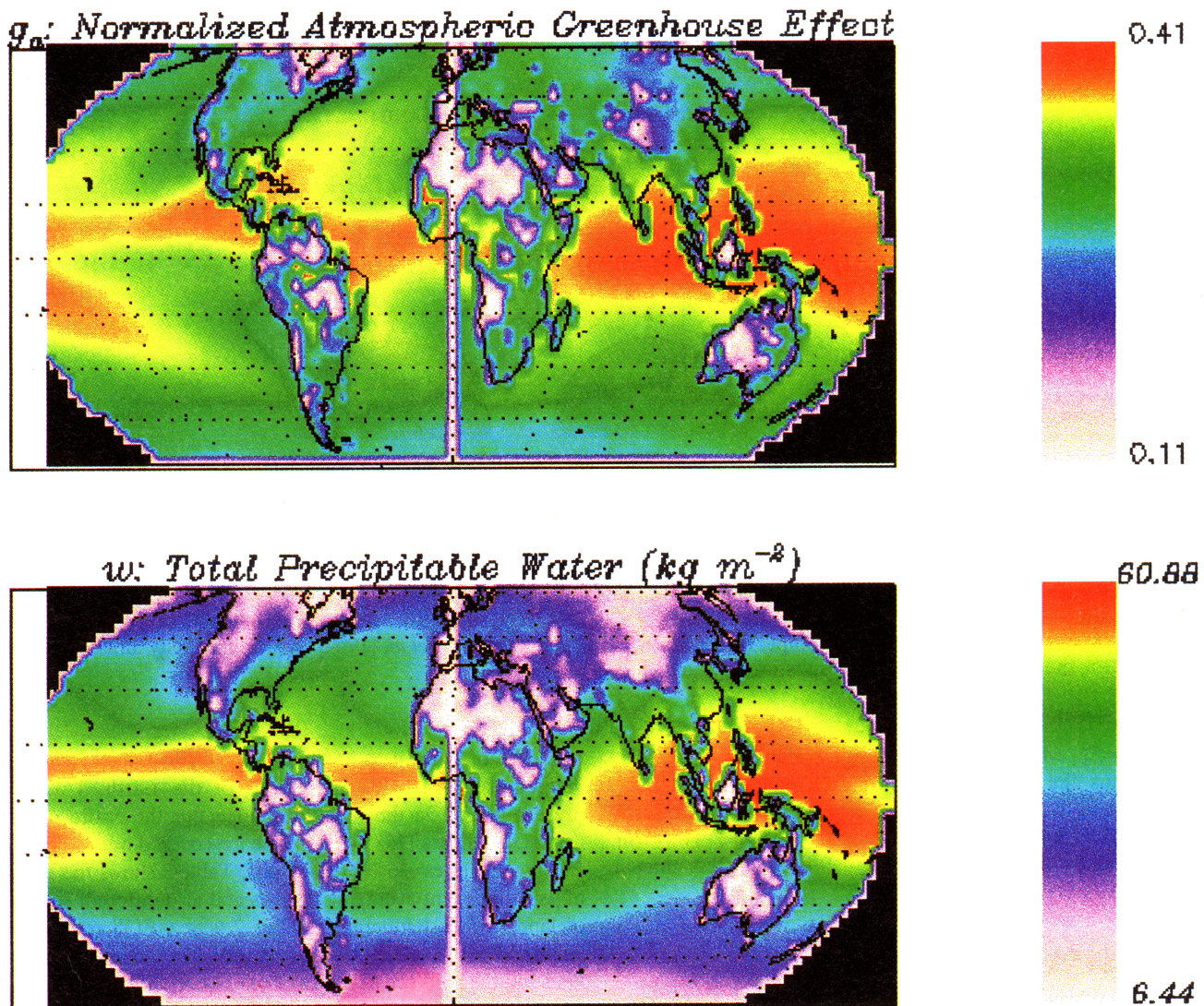
Plate 1. (top) Regional distribution of the annual mean atmospheric greenhouse effect (g_a) from 1988 and 1989 data. (bottom) Regional distribution of the annual mean total precipitable water w from 1988 and 1989 NVAP (NASA water vapor project) data.

variations in atmospheric humidity and lapse rates. As shown in Plate 1, g_a increases from pole to equator largely because of the increase in humidity (shown in the bottom panel) from pole to equator [*Stephens et al.*, 1991; RR]. Furthermore, for the same latitude zone, the continental g_a values are significantly lower than the ocean values, indicating that the land regions are drier than the oceanic regions.

As shown by RR and *Stephens* [1990], geographical variations in g_a are dominated by the dependence of g_a on water vapor (w) and T_S; that is, g_a increases with w which in turn increases with T_S. The equator to pole decrease in g_a is largely due to the corresponding decrease in T_S and w. However, the atmospheric dynamics also has a strong influence on g_a. We use maps of the regional distributions of g_a (top panel) and total precipitable water w (bottom panel) to illustrate the role of dynamics of water vapor transport and its interaction with the greenhouse effect.

We can distinctly see enhanced values of g_a (top panel) and w (bottom panel) in the deep convective regions of the western Pacific, the Intertropical Convergence Zone (ITCZ), including the slightly northward shifted ITCZ contour in the east Pacific

and the Atlantic, surrounded by lower values of g_a in the subtropical high-pressure belt with strong subsidence. The subsidence over the desert regimes of North Africa (Sahel Desert), South Africa (Kalahari Desert), Asia (Gobi Desert), South America, and Australia are quite marked. These regions are characterized by very low surface emissivities (significantly below 1) and low precipitable water amounts (bottom panel of Plate 1) causing an anamolously low greenhouse effect. Lastly, the data displayed in the two panels of Plate 1 reveal a remarkable consistency between regional variations in g_a and w; that is, regions with enhanced g_a also have higher w. This consistency between the radiometric and the water vapor data sets is important for the feedback analyses presented in section 5.

5. Annual Cycle on Tropical and Global Scales

The north to south averaged annual cycles of T_S, g_a, and precipitable water (w) are shown, respectively, in Figures 3a, 3b, and 3c for the tropics (30°N–30°S) and in Figures 4a, 4b, and 4c for the globe (90°N–90°S). The precipitable water w is resolved into three tropospheric layers: w_1 for lower (surface
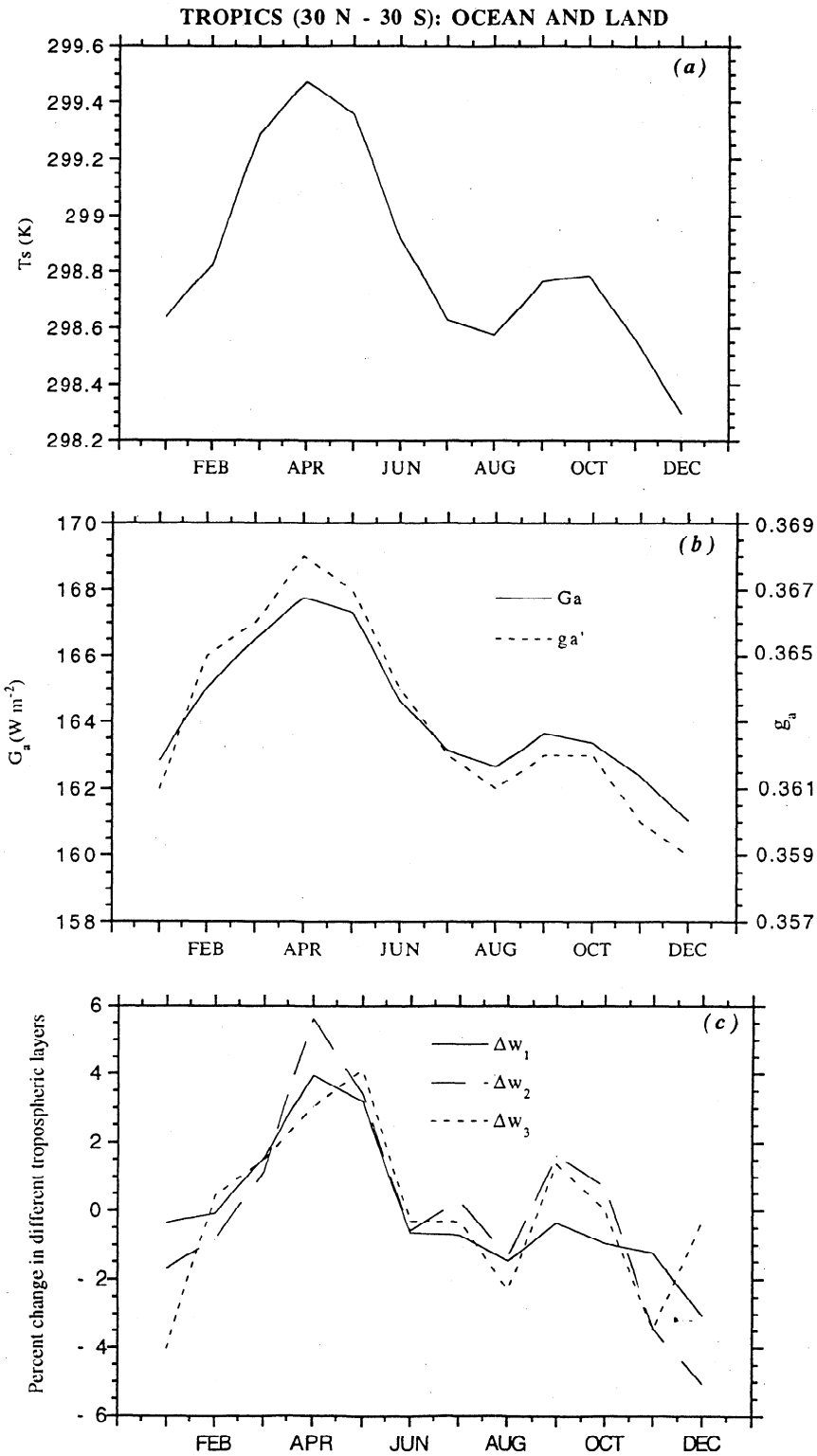
Figure 3. Annual cycles for the tropics (30°N–30°S). (a) surface temperature (T_S) obtained from the same sources as in Figure 2; (b) atmospheric greenhouse effect (G_a) and the normalized atmospheric greenhouse effect g_a shown by dashed line; and (c) percent change in precipitable water in three tropospheric layers, namely lower (w_1 between surface and 700 mbar), middle (w_2 between 700 and 500 mbar), and upper (w_3 between 500 and 300 mbar).
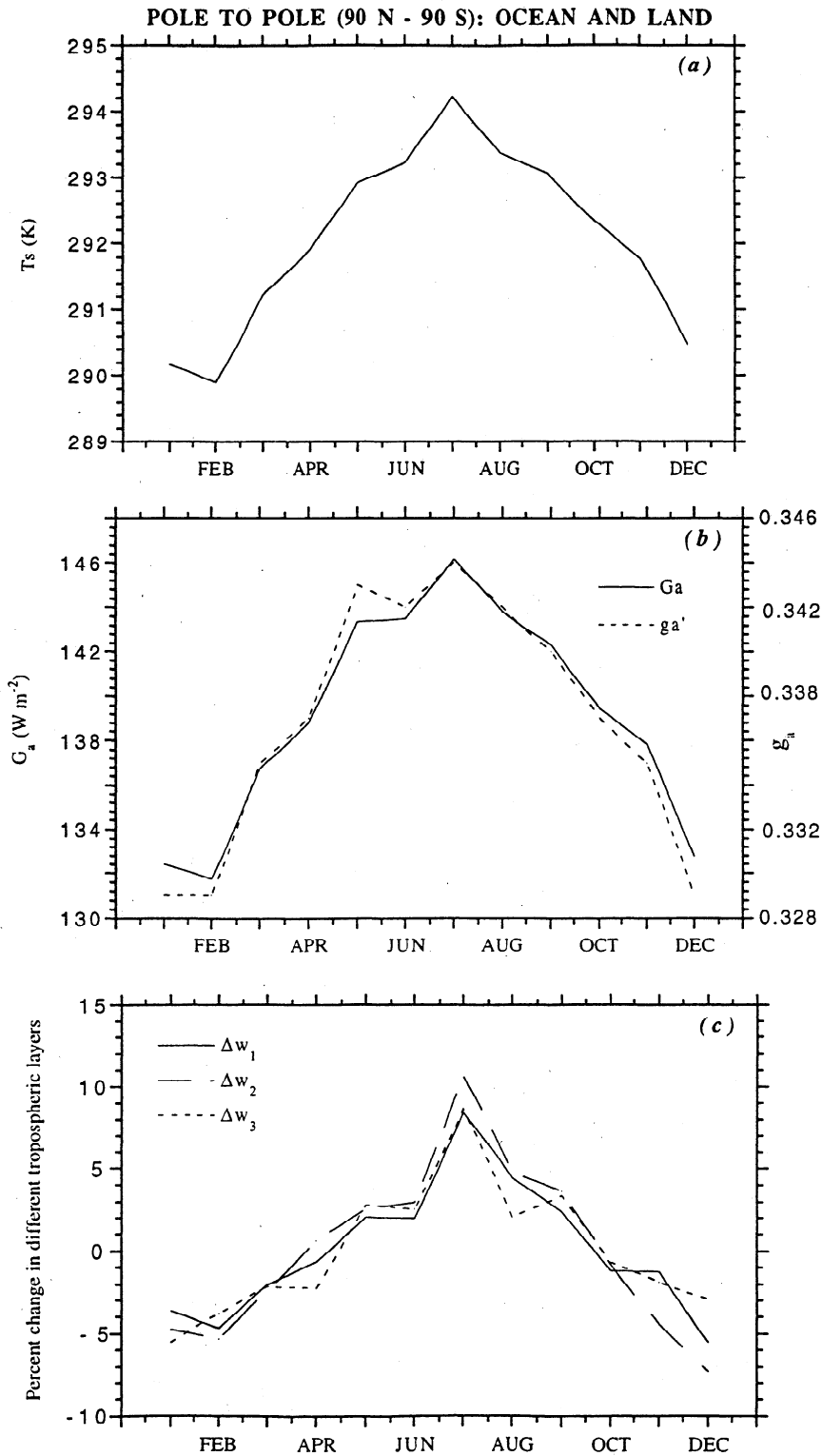
POLE TO POLE (90 N - 90 S): OCEAN AND LAND

Figure 4. Same as Figure 3 but for 90°N–90°S.

to 700 mbar), w_2 for middle (700–500 mbar), and w_3 for upper (500–300 mbar) troposphere.

Why should the planet as a whole exhibit an annual cycle? Among the many probable contributing factors, three obvious candidates are as follows: (1) the solar insolation averaged over the planet peaks in December 21 and has a minimum on June 21 due to the eccentricity of the orbit. The amplitude of this cycle is 12 W m^{-2}, which is 3.5% of the mean value of 342 W m^{-2}; (2) the north-south asymmetry in the land fraction would by itself contribute to an annual cycle even in the absence of eccentricity changes; and (3) north-south asymmetries in atmospheric and oceanic circulation arise from the above two factors.

For the tropics, T_S peaks in March/April, while for 90°N–

90°S, T_S peaks in July. We can qualitatively interpret the phase of the annual cycle as follows:

The tropical annual cycle is dominated by the coupled ocean-atmosphere system, and as a result, the temperature response lags behind the forcing by a maximum of about 3 months ($\pi/2$); thus with the solar insolation peaking in December 21, the temperature peaks in late March, as shown in Figure 3. In addition to the annual cycle, the figure also reveals a semiannual cycle, whose amplitude is comparable to the annual cycle amplitude.

The extratropical and global annual cycle is most likely dominated by the hemispherical asymmetry in the land fraction. During the northern hemisphere summer (June, July, and August) the large landmasses warm rapidly (with about a 1 month lag), which dominates the hemispherical and global mean response; however, during the southern hemisphere summer the relatively smaller fraction of land prevents a corresponding response. Thus the globe is warmest during June/July and is coldest during December/January.

Both Figures 3 and 4 reveal that g_a, w_1, w_2, w_3, and T_S are positively correlated. The figures again reveal the consistency between the radiation budget data and water vapor data. When w and g_a are correlated with T_S, the best correlation coefficient is obtained for a phase lag of less than a month (as shown later). This near-zero phase lag rules out the possibility of variations in g_a or w driving variations in T_S; were this to be

Water Vapor Feedback Sensitivity (Ocean + Land): dF_c/dT_s
30 N – 30 S

SLOPE 0.30 W m^{-2} K^{-1}

90 N – 90 S

SLOPE 2.11 W m^{-2} K^{-1}

Figure 6. Same as in Figure 5 but for F_C versus T_S.

the case, T_S should lag behind the forcing by at least more than a month. On the other hand, since convective timescales are less than a month, it is reasonable to expect that variations in g_a and w are driven by variations in T_S without much phase lag. The deduction is that the correlation coefficient between g_a and T_S or that between w and T_S is the feedback parameter, valid, at least for annual timescales.

6. Feedback Analyses

6.1. Tropical and Global G_a-T_S Correlations

Scatterplots of G_a versus T_S for the tropics (30°N–30°S) and globe (90°N–90°S) are shown in Figures 5a and 5b, and similar plots of F_C versus T_S are shown in Figures 6a and 6b. The feedback term dG_a/dT_S derived from the annual and interannual cycles of monthly mean values are plotted in Figures 7 (ocean and land) and 8 (ocean only) as a function of the latitude range from pole to pole. The $G_a - T_S$ correlation was performed by successively including larger domains, extending in increments of 5° on either side of the equator (e.g., 5°N–5°S, 10°N–10°S, and so on). The domain-averaged $\langle G_a \rangle$ is obtained, as described previously from the corresponding domain-averaged surface temperature and OLR as

$$\langle G_a \rangle = \sigma \langle T_S \rangle^4 - \langle F_C \rangle$$

The period 1985–1987 was marked by ENSO which peaked with the El Nino event in 1987. Since the annual cycle signals were weak during this ENSO, we employ only the years 1988–1989 for the correlation analysis here. The solid line depicted

Water Vapor Feedback Sensitivity (Ocean + Land): dG_o/dT_s
30 N – 30 S

SLOPE 5.76 W m^{-2} K^{-1}
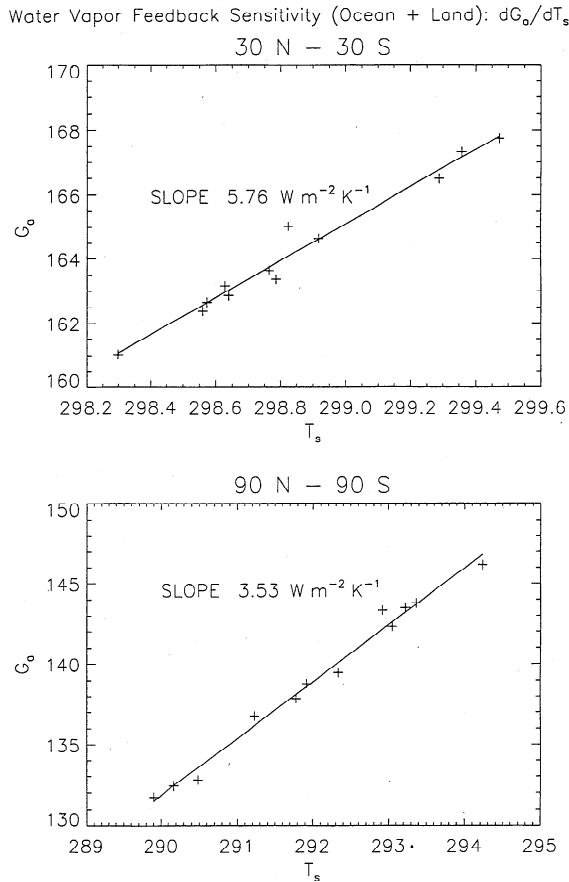
90 N – 90 S

SLOPE 3.53 W m^{-2} K^{-1}

Figure 5. Scatterplots of G_a versus T_S using the annual cycles shown in Figures 3 and 4 for the two domains (i.e., 30°N–30°S and globe). The slope dG_a/dT_S, representing the water vapor feedback sensitivity parameter, obtained from the least squares fit of the data, is inset in the figures.
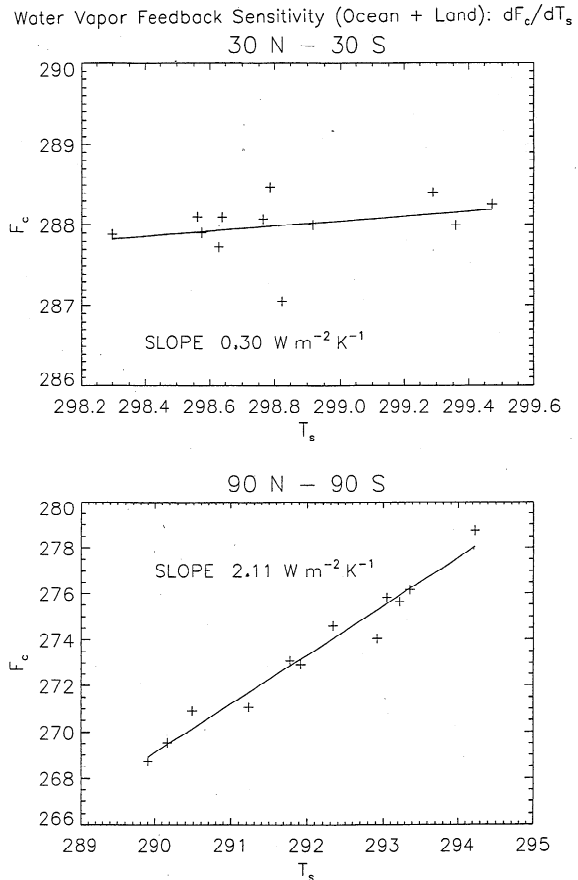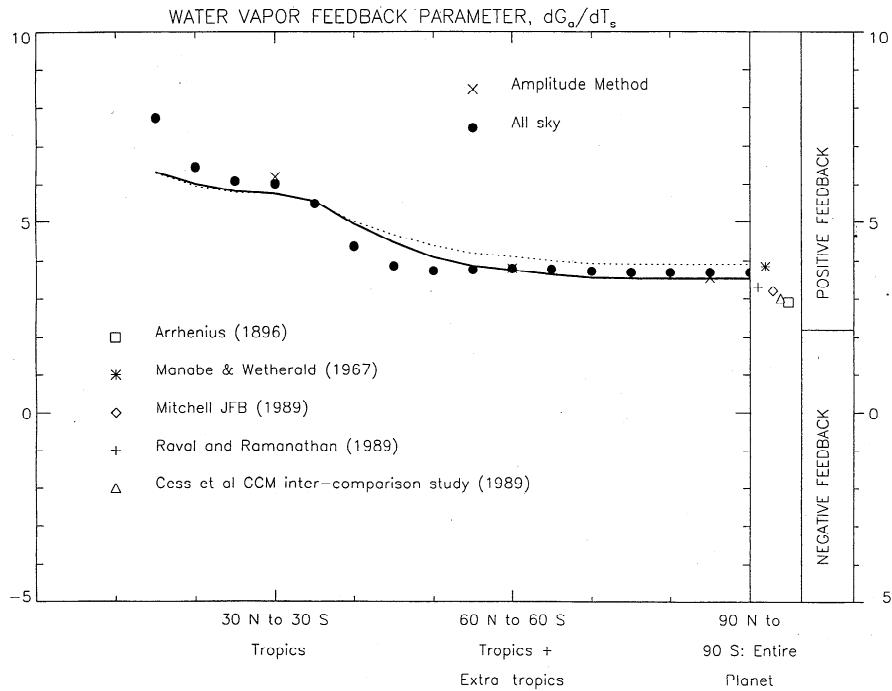
Figure 7. Feedback sensitivity parameter dG_a/dT_S for different latitude ranges (ocean plus land). The solid line depicts results which use the station data for the land surface temperatures (1988–1989), while the dashed line employs the GEOS data. The results derived from the amplitude method (see text), and also the ERBE all-sky OLRs are shown by symbols. The equivalent estimates for the globe from other studies and GCM simulations are shown in the second right box, while the box at the extreme right marks the range of dG_a/dT_S into regions of positive and negative feedback.
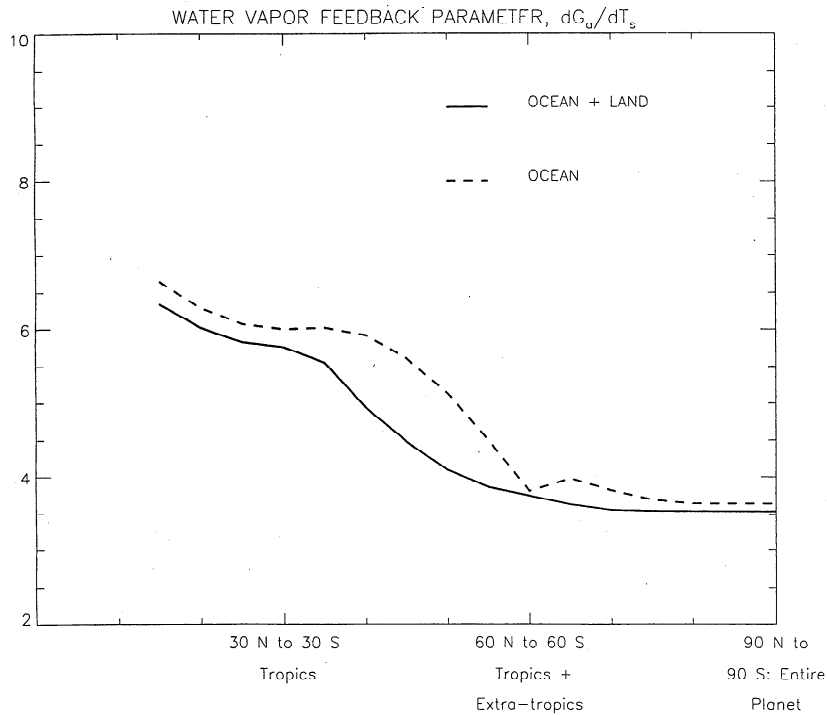

Figure 8. Feedback sensitivity parameter dG_a/dT_S for different latitude ranges for the ocean and ocean plus land, shown separately.

in Figure 7 has been derived using the annual cycle from station data, while the dashed line is derived employing the GEOS surface temperature data. Focusing first on the clear-sky sensitivity values (as opposed to the all-sky values shown by circles), we infer the following features from Figure 7:

1. Between 10°N and 10°S (not shown), dG_a/dT_S (7–10 W m^{-2} K^{-1}) exceeds the blackbody emission value of about 6 W m^{-2} K^{-1}, thus reproducing the so-called super greenhouse effect inferred from latitudinal variations in G_a and T_S (RR) and from El Nino-induced variations [*Ramanathan and Collins*, 1991]. The large value of dG_a/dT_S is due to the increase in frequency of convection with T_S [*Waliser et al.*, 1993] and the subsequent increase in middle and upper tropospheric water vapor [*Hallberg and Inamdar*, 1993]. We have to bear in mind, however, that both temperature effect (as represented by the Planck and lapse rate feedbacks) and moisture feedbacks contribute to the observed dG_a/dT_S, as can be inferred from (4) [also see *Inamdar and Ramanathan*, 1994]. The role of the lapse-rate feedback is discussed further at the end of this section.

2. Away from the equatorial regions, dG_a/dT_S decreases rapidly and asymptotes to the global mean value of about 3.5 W m^{-2} K^{-1}. The enhanced trapping in the equatorial regions is compensated by enhanced emission to space from the subtropics and the extratropics. The enhanced emission in the subtropics is most likely due to the drying effect of deep convection (as evidenced from the all-sky flux changes discussed later); in the extratropics, on the other hand, temperature changes are confined largely to the northern hemisphere land regions, which are not so effective as oceanic regions in enhancing water vapor in the atmosphere (this point is discussed in detail later).

3. Upon comparing with the all-sky values, we see that the cloud longwave forcing feedback term does not contribute to the global sensitivity. This does not, however, imply that clouds do not change. In fact, in the equatorial regions, the all-sky sensitivity is much larger, thus indicating a large increase in convective clouds. In the subtropical regions however, the drying effect of increased equatorial convection decreases the sensitivity to very close to clear-sky values.

In summary, the data reveal the subtropical drying effect of deep convection, qualitatively similar to that suggested by *Lindzen* [1990]; but unlike Lindzen's mechanism, the drying effect is not sufficiently large and the positive water vapor feedback dominates in the tropics. One possible reason is the failure of Lindzen's mechanism to account for the large super greenhouse effect in the low latitudes.

In Figure 8 we compare the land plus ocean sensitivity with the ocean-only sensitivity to understand the role of the land surfaces. At all latitudes the ocean sensitivity is larger, thus suggesting that the drying effect may be happening more over the land.

To test the robustness of the analysis, we employed another independent method, denoted in Figure 7 as the "amplitude method." Here we performed a Fourier decomposition of the time series of surface and atmospheric temperatures and the atmospheric greenhouse effect for the tropics (30°N–30°S), 60°N–60°S, and also the globe, extracting the amplitude and phase for both parameters. The values marked in Figure 7 have been derived by taking the ratio of the respective first harmonic amplitudes. Again, the results from the "amplitude" method are identical with the other methods.
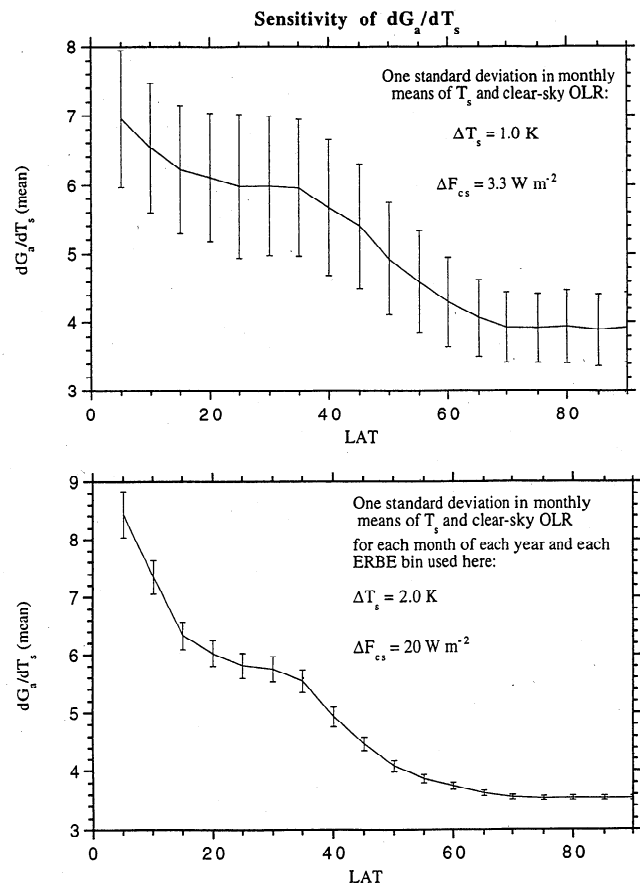

Figure 9. Error bars for the dG_a/dT_S, due to one standard deviation error in T_S and OLR applied uniformly over a spatial domain (top) and distributed randomly among the individual ERBE bins (bottom).

6.2. Error Analysis

To further assess the effect of data uncertainties in the sensitivity estimates, we performed an error analysis of the dG_a/dT_S term by accounting for random errors in the OLR and T_S, the two parameters that are needed in the analysis. To do this, different sets of normally distributed random numbers with mean zero and a standard deviation of 1 K for T_S and 3.3 W m^{-2} for OLR [*Wielicki et al.*, 1995] have been generated to simulate the errors in T_S and OLR. In the first method (top panel of Figure 9), the errors are assumed to apply uniformly for the entire spatial domain considered. In the second method, errors are considered on the ERBE grid scale and assumed to be spatially uncorrelated. Inspite of the higher estimates of standard deviations used as inset in Figure 9, uncertainties are very small. The uncertainties are larger for the first method but diminish significantly on a global basis.

7. Implications to the Role of Water Vapor Feedback in Global Warming

7.1. Comparison of the Sensitivity Parameter With Other Studies

In Figure 7 we compare the annual cycle sensitivity with those inferred from available model studies dealing with the global warming due to increased CO_2. *Arrhenius* [1896] was perhaps the first to account for the water vapor feedback. In a

recent study by *Ramanathan and Vogelmann* [1997] it is shown that water vapor feedback amplifies the surface warming by a factor of 1.3 in the Arrhenius model. We can translate this into a dG_a/dT_S estimate as follows:

If F denotes OLR, and $\Delta f = $ OLR, sensitivity to surface temperature change = 3.3 W m^{-2} K^{-1} without H$_2$O feedback [from *Cess*, 1990], then using $\Delta T_S = \Delta f/(dF/dT_S)$, we get $dF/dT_S = 3.3/1.3 = 2.54$ W m^{-2} K^{-1}.

Since $G_a = \sigma T_S^4 - F$, it follows

$$dG_a/dT_S = 4\sigma T_S^3 - dF/dT_S = 5.42 - 2.54$$

$$\approx 2.9 \text{ W m}^{-2} \text{ K}^{-1}.$$

This value is in the lower range of estimates shown in Figure 7.

The first study to use the concept of a water vapor feedback in a radiative-convective model was that of *Manabe and Wetherald* [1967]. A subsequent general circulation model (GCM) study [*Wetherald and Manabe*, 1975] analyzed the sensitivity of GCMs outgoing longwave flux to a 2% increase in the solar flux, which yielded values consistent with those of the earlier radiative-convective model. The corresponding dG_a/dT_S estimate from their study turns out to be 3.7 W m^{-2} K^{-1}, which is very close to our estimates from the ERBE data shown in Figure 7.

Mitchell [1989] in his study of climate feedback mechanisms, derived an average estimate for the water vapor feedback factor from analyzing the results of CO$_2$-doubling experiments using both radiative-convective and three-dimensional climate models. His feedback-corrected estimates of longwave cooling to space of 2.2 W m^{-2} K^{-1} transform to a dG_a/dT_S value of about 3.3 W m^{-2} K^{-1}, which is again close to the earlier estimate.

Raval and Ramanathan [1989] estimated the relationship among atmospheric greenhouse effect, surface temperature, and precipitable water vapor from observational data. They provided an estimate of 3.3 W m^{-2} K^{-1} for G_a sensitivity from the ERBE measurements over the oceanic regions of the globe.

Finally, *Cess et al.* [1990], in their intercomparison study of global warming simulations from 19 GCMs, found excellent agreement among their depictions of OLR sensitivity to surface temperature increase with a mean value for dF/dT_S of 2.34 W m^{-2} K^{-1} and a standard deviation of 0.2 W m^{-2} K^{-1}. This is in spite of the 19 GCMs using several different parameterization schemes for convection, thus confirming that their agreement over water vapor feedback is not an artefact of this parameterization.

In summary, it is shown that the G_a sensitivity derived from several approaches (GCMs and observations from independent sources) all converge in the range of 2.9–3.8 W m^{-2} K^{-1} for the globe. As derived earlier, the threshold level for positive feedback is given by $dG_a/dT_S > 2.2$ W m^{-2} K^{-1}. The boundaries of positive and negative feedback are marked separately in Figure 7.

7.2. Relevance of the Annual Cycle to Global Warming

The magnitude of dG_a/dT_S is governed by changes in atmospheric lapse rate and in humidity (q). The similarity of changes in q and lapse rate between the annual cycle changes and the longer-term (say decadal) climate changes is an indicator of the relevance of the feedback inferred from the annual cycle to global warming. For the annual cycle we examine the difference between the warmest and the coldest 3 month av-

erages. For the longer term we adopt published decadal-scale-observed changes [*Angell*, 1988; *Oort and Liu*, 1993] and GCM results for doubling of CO$_2$ (as reported in *IPCC* [1995]).

7.2.1. Tropical region between 30°N and 30°S.
The annual cycle peaks during the spring months (March-April-May) for the tropics (see Figure 3). Figure 10a and 10b present the average difference between the warm (MAM) and the cold (DJF) months of the cycle of surface temperatures (extracted from GEOS) and corresponding percent change in column-integrated water vapor in the three tropospheric layers (surface to 700 mbar, 700–500 mbar, and 500–300 mbar) derived from the NVAP water vapor data. Figures 10a and 10b include only the oceans (without sea ice), while Figure 10c and 10d present the same for the land and ocean combined case. The dotted lines in Figures 10b and 10d represent the column precipitable water when the relative humidity is conserved. We refer the reader to our comment in an earlier section on the procedure adopted to obtain the domain averages.

The ΔT decreases with altitude (Figure 10a). Observed decadal timescale temperature changes [*Angel*, 1988; *Oort and Liu*, 1993], on the other hand, reveal that tropical tropospheric temperature changes are nearly constant with altitude. GCM studies of global warming during the last century, on the other hand, contradict both the annual cycle and the decadal-scale changes by estimating an upper tropospheric warming that is about 30–50% larger than the surface temperature changes [e.g., *IPCC*, 1995]. At least part of this warming may be due to the neglect of the ozone-induced lower stratospheric/upper tropospheric cooling in the GCMs [*IPCC*, 1995].

Observed humidity changes (shown in percent in Figure 10b) are very close to the values we would expect for a constant relative humidity atmosphere for the lower troposphere, while they exceed those values significantly in the middle and upper troposphere. Figures 10b and 10d strongly suggest that the midtropospheric layers of the deep convective regions in the tropics undergo a significant moistening consistent with the study of *Hallberg and Inamdar* [1993]. These results are also consistent with the decadal-scale tropical humidity changes reported by *Hense et al.* [1988] and *Flohn and Kapala* [1989]. However, they are inconsistent with the results reported by *Schroeder and McGuire* [1998]. This study reports a tropical drying during the 1989–1995 period, in spite of the surface warming during the same period. However, the 1990s period was also subject to frequent El Ninos, and we have to separate the El Nino effect from that of the global warming, before interpreting decadal trends. Furthermore, Schroeder and McGuire use water vapor amount from soundings retrieved from satellite infrared data which seem to be at variance with NVAP results given by *Randel et al.* [1996]. The NVAP incorporates water vapor column amount from satellite microwave data and sondes, in addition to the satellite infrared soundings. *Randel et al.* [1996] examine the global trend between column water vapor and surface temperature for the 1988 to 1993 and conclude that their results "confirm the physical principle that a warmer atmosphere contains more water vapor than a cooler one." Lastly, the NVAP data reveal a marked decrease in water vapor column amount beginning in 1991, while the Schroder and McGuire data show this marked decrease to begin in 1988. Clearly, long-term trends from satellite water vapor column data need more scrutiny for accuracy before making a definite statement.

7.2.2. Extratropical and global scales.
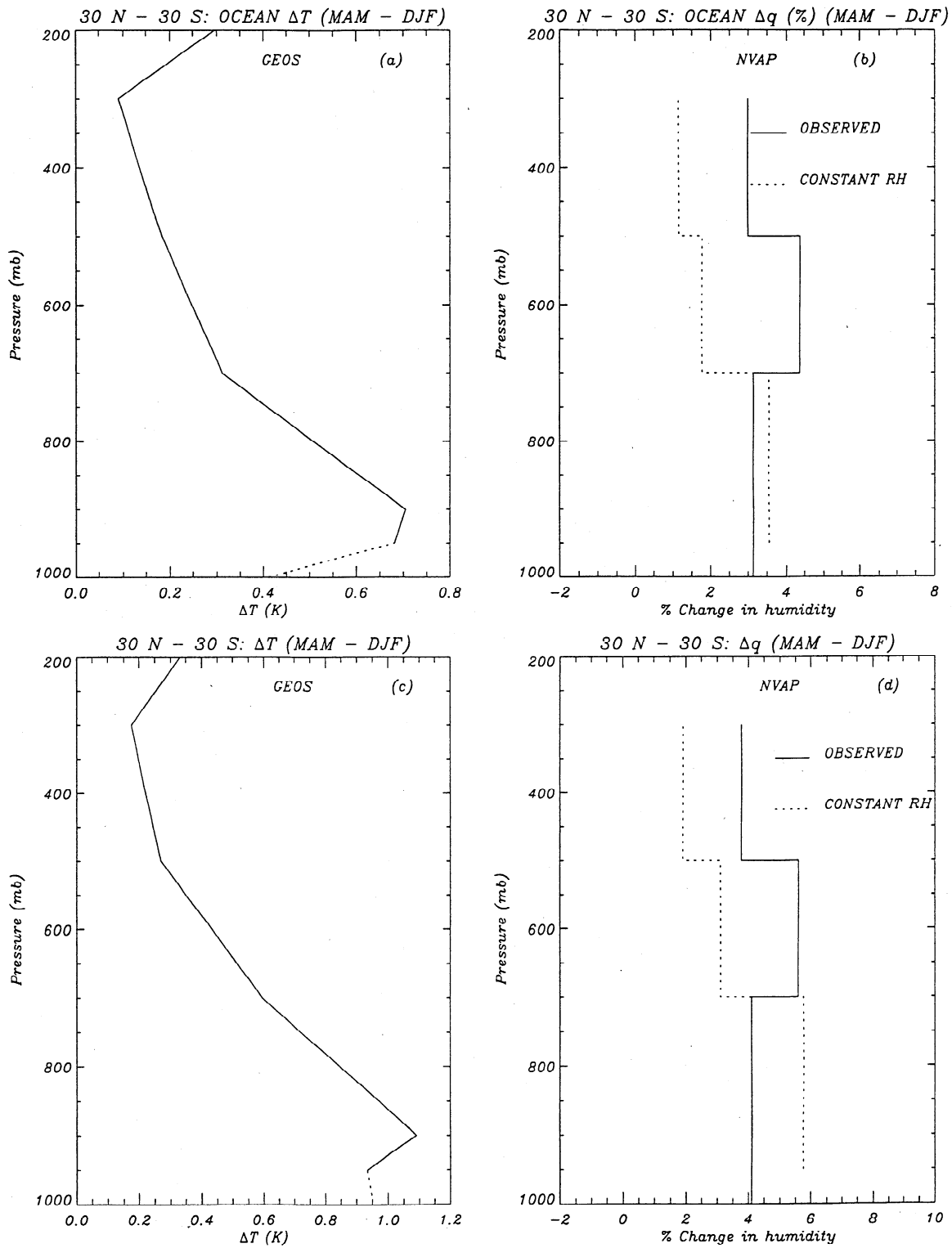Figures 11a–11d depict changes analogous to Figure 10a but on a global scale

Figure 10. (a) Vertical distribution of atmospheric temperature changes obtained by differencing the MAM and DJF values for the tropical oceans (30°N–30°S); (b) same as Figure 10a but for atmospheric humidity mixing ratio (q); (c) same as Figure 10a but for the ocean and land combined; (d) same as Figure 10b but for the ocean and land combined. The dotted lines in Figures 10b and 10d represent the constant relative humidity.
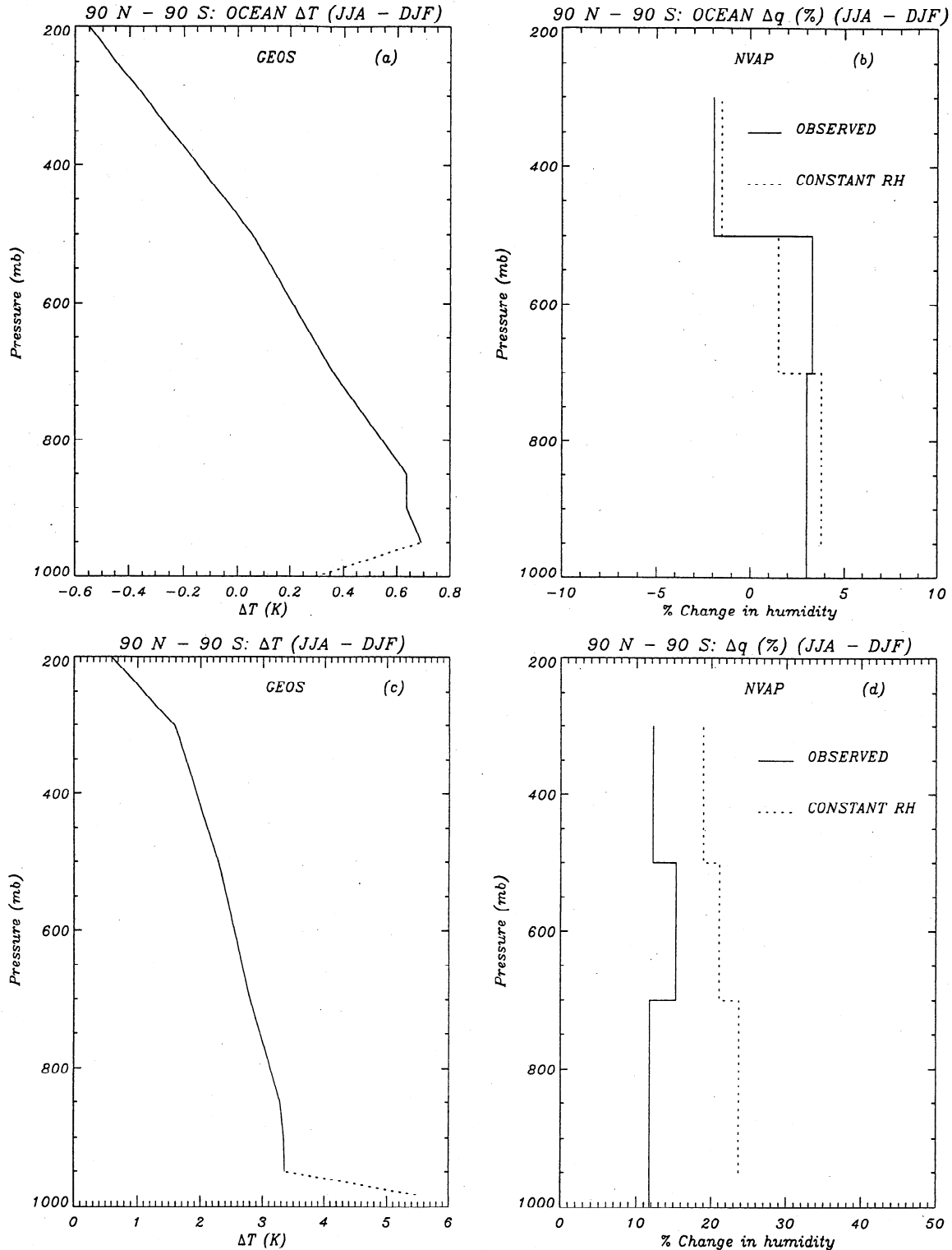
Figure 11. Same as Figure 10 but for the globe (90°N–90°S), except the changes in atmospheric temperature and humidity have been obtained by differencing the JJA and DJF values.

(90°N–90°S). The warmest and coldest months are JJA and DJF consistent with the seasonal cycle shown in Figure 4. The atmospheric temperature (Figure 11a) decreases steeply with altitude, contrary to the near-uniform vertical temperature changes associated with either the observed decadal scale vari-

ations [*Angel*, 1988; *Oort and Liu*, 1993] or the GCM response to increased CO_2. The humidity increases over the global oceans (Figure 11b) are close to constant relative humidity values through the troposphere.

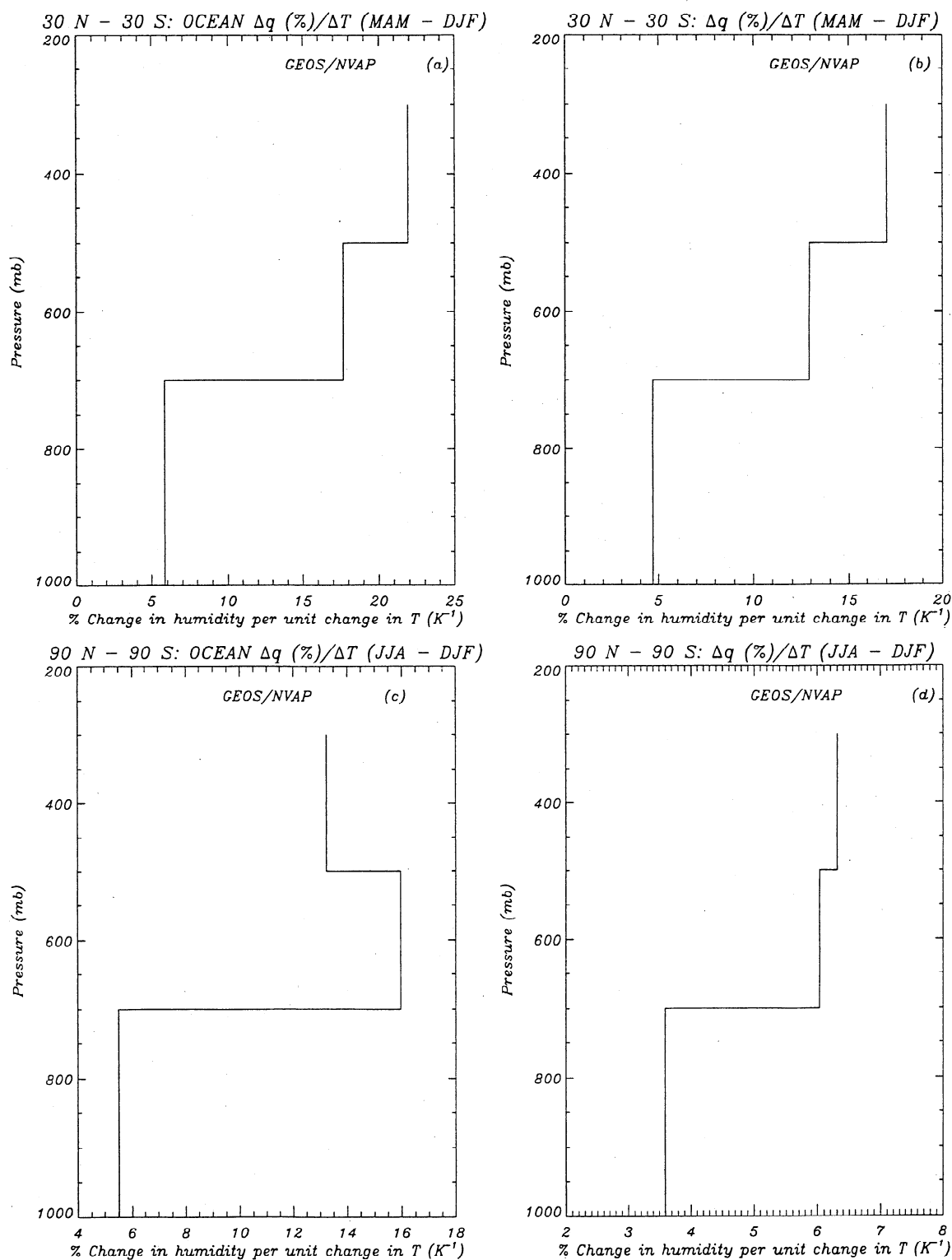For the combined land and ocean, however, the increases in

Figure 12. Vertical distribution of the ratio of the change in water vapor mixing ratio (%) and the layer-averaged atmospheric temperature. (a) Tropical oceans; the Δq and ΔT values are obtained by differencing the MAM and DJF values; (b) combined ocean and land for the tropics; the Δq and ΔT values are obtained by differencing the MAM and DJF values; (c) global oceans; the Δq and ΔT values are obtained by differencing the JJA and DJF values; (d) combined ocean and land for the globe; the Δq and ΔT values are obtained by differencing the JJA and DJF values.

humidity (Figure 11d) are significantly smaller when compared with the constant relative humidity case. The reason for this becomes obvious when we inspect the temperature changes shown on the left-hand panel. The ocean temperature changes are about a factor of 10 smaller than the combined land and ocean case, thus indicating that temperature changes over land (and that too in the northern hemisphere) dominate the total changes. The primary source of evaporation, however, is the oceans where temperature increases are smaller. As a result, the combined land and ocean evaporation increases are not so large as that dictated by temperature increases. Since evaporation is the fundamental source of atmospheric moisture, the moisture increase for the combined land and ocean is smaller. This result is a valuable reminder for the importance of the oceans in the water vapor feedback.

Figure 12 shows the increase in humidity (%) in each of the three tropospheric layers per degree change in temperature of the respective layer. This is yet another way of summarizing the results shown in Figures 10 and 11. For the tropical region (ocean or ocean plus land), the midtropospheric humidity increases by as much as 15–20% per degree increase in temperature. This should be compared with the 20% per degree warming increase in midtroposphere humidity reported by *Hense et al.* [1988] and *Flohn et al.* [1989] for decadal-scale trends. We see that in spite of the domain, the altitude or the region, humidity changes are always positively correlated with temperature changes. The same conclusion was reached by *Gaffen et al.* [1991] in their study of decadal timescale changes in humidity.

The magnitude of the changes shown in Figure 12 can be approximately explained from the temperature dependence of the Clausius-Clapeyron equation. The saturation vapor pressure e_S can be expressed as

$$e_S \approx C \exp{(-5400/T)}$$

where C is a constant. Upon differentiating e_S with respect to T, we obtain

$$\frac{1}{e_S}\frac{de_S}{dT}(\%) = \frac{5400}{T^2} \times 100$$

For $T \approx 300$ K, the above expression yields 6% K^{-1}, while for $T \approx 200$ K, it yields about 13% K^{-1}. Thus the increase with altitude of the percent change in q can be related to the temperature dependence of e_S. However, an explanation for the atmosphere's tendency to maintain constant relative humidity must include the role of the dynamics in water vapor transport.

In summary, lapse rate changes for the annual cycle are not a valid analog for longer timescale climate changes. However, for reasons given below, the discrepancy in lapse rate changes between observations and GCMs do not alter our conclusion on the role of water vapor feedback. The observed annual cycle warming decreases with altitude, the decadal-scale warming remains roughly constant with altitude, while the GCM warming increases with altitude. When atmospheric warming is not so large as the surface warming, the enhanced emission to space is not so large (when compared with the situation when the warming is about the same at all altitudes), which in turn enhances dG_a/dT_S, i.e., a positive feedback. However, at the same time, in a fixed relative humidity environment, smaller atmospheric warming implies a smaller increase in absolute humidity, which suppresses some of the increase in dG_a/dT_S

from the lapse rate feedback. Because of these two competing effects, the lapse rate (changes shown in Figure 10) has less than 10% influence on dG_a/dT_S.

Humidity increases, on the other hand, are mostly consistent with available studies on observed longer timescale changes and with GCM studies. The one apparent exception is the global mean combined land and ocean case, for which humidity changes are about 50% of the values expected for an atmosphere with fixed relative humidity. However, surface temperature changes for this case are mostly concentrated in the northern hemisphere land. Inspite of such heterogeneous and hybrid temperature changes, the observed dG_a/dT_S values are without exception consistent with positive water vapor feedback.

It is for this reason that we conclude that any theories or models that propose to simulate global warming should be tested against the data presented here. Agreement with the dG_a/dT_S values shown here, by itself, does not guarantee an accurate prediction of global warming, but failure to reproduce the present results or a substantial discrepancy with the sensitivity values shown here provide sufficient justification to question the theory.

8. Summary and Conclusions

We have revisited the issue of water vapor feedback employing a multitude of data sets presently available. Major objectives of the study are to integrate the presently available data sets, discuss the limitations of the previous studies, and address specific issues that were the stumbling blocks toward a reliable estimation of water vapor feedback on a global scale.

The present analysis covers the entire globe, including oceans and land surfaces. Mutual compatibility between data sets from independent sources and their influence on the results have been assessed. Regional and global average values for the different radiative flux parameters have been derived using the ERBE and other data sets. Maps of regional distributions of g_a and w values display a remarkable consistency and qualitatively portray the role of large-scale dynamic water vapor transport on atmospheric greenhouse effect.

The annual cycles are then examined to infer the water vapor feedback sensitivity factor dG_a/dT_S. G_a, w, and T_S have been found to be highly correlated consistent with the earlier study of RR, even when the analysis is extended in geography and time. The feedback sensitivity parameter dG_a/dT_S tracks the response of equatorial convection and large-scale circulation of water vapor and its greenhouse effect. In particular, we note the following features: (1) increase in equatorial convection in response to warming, moistens the midtroposphere between 10°N and 10°S and contributes to the so-called super greenhouse effect; (2) the Hadley cell response to the equatorial convection is to dry the subtropics and extratropics, which compensates for some of the enhanced equatorial greenhouse effect; (3) on tropical and global scales, however, there is a net moistening effect, and the feedback is positive and is similar to that of the fixed relative humidity models. Results derived for the feedback sensitivity parameter from different methods of analysis or use of different independent data sets, as well as those from other studies and GCM simulations, all converge within a ±20% range. Interestingly, the atmospheric precipitable water also shows a similar response to the surface temperature. Presence of deep convective regions in the tropics causes a large convergence of water

vapor in the midtroposphere. Our results also show that the response of the vertical water vapor concentration over the tropical and global oceans is similar to that expected from a fixed relative humidity atmosphere.

Lacking a long record of the satellite observations of the Earth, we have attempted to use the seasonal and interannual changes as a surrogate data. The results are fully consistent with observations and GCM simulations and suggest a positive water vapor feedback on tropical and global scale (Figure 7). In this context, *Lindzen* [1990, 1994] hypothesized that more and deeper cumulus convection expected in a warmer climate will lead to drying of the middle to upper troposphere, resulting in a significant reduction in the atmospheric greenhouse effect due to water vapor and thus ameliorating the effect of CO_2 warming. He estimated a response of 0.35°–1°C warming due to doubling of CO_2, which is well below the IPCC projections. Lindzen's estimates translate into a feedback sensitivity (dG_a/dT_S) in the range of -4.5 to -1 W m^{-2} K^{-1}. This falls in the domain marked as negative feedback in Figure 7 and is not supported by the present radiometric data. When this result is combined with the findings of earlier studies [*Inamdar and Ramanathan*, 1994; *Soden et al.*, 1995; *Flohn et al.*, 1989] that deep convection enhances the middle and upper tropospheric moisture; and that increased frequency of deep convections during El Nino year [*Ramanathan and Collins*, 1991; *Soden*, 1997] enhances the greenhouse effect with greater effect on regional and tropical mean scales, it may be concluded that the cumulus drying hypothesis of *Lindzen* [1990] does not explain tropical or global scale annual (and decadal) changes in water vapor and atmospheric greenhouse effect in the present atmosphere. By deduction, its validity for the global warming problem is in doubt.

Although we have used several different sources of data and where appropriate attempted to check for mutual compatibility, one need not stress more about the need for a continuous and accurate data record of radiative energy balances in the atmosphere. The Cloud and Earth Radiant Energy Systems (CERES) is one such instrument to be flown aboard the TRMM satellite this year and to be followed up with the EOS platforms later. With its broadband and window longwave channels, and other spectral instruments which measure the surface characteristics like emissivity, it should fulfill the above needs of providing a near-global coverage and help in detecting trends in the greenhouse effect in response to anthropogenic influences.

References

Angell, J. K., Variations and trends in tropospheric and stratospheric global temperatures, 1958–87, *J. Clim.*, *1*, 1296–1313, 1988.

Arrhenius, S., On the influence of carbonic acid in the air upon the temperature of the ground, *Philos. Mag.*, *41*, 237–276, 1896.

Barkstrom, B. R., The Earth Radiation Budget Experiment (ERBE), *Bull. Am. Meteorol. Soc.*, *65*, 1170–1185, 1984.

Barkstrom, B. R., E. F. Harrison, G. L. Smith, R. Green, J. Kibler, R. Cess, and the ERBE Science Team, Earth Radiation Budget Experiment (ERBE) archival and April 1985 results, *Bull. Am. Meteorol. Soc.*, *70*, 1254–1262, 1989.

Bengtsson, L., A numerical simulation of anthropogenic climate change, *Ambio*, *26*, 58–65, 1997.

Bony, S., J. P. Duvel, and H. L. Treut, Observed dependence of water vapor and clear-sky greenhouse effect on sea surface temperature: Comparison with climate warming experiments, *Clim. Dyn.*, *11*, 307–320, 1995.

Cess, R. D., Gauging water vapor feedback, *Nature*, *342*, 736–737, 1991.

Cess, R. D., et al., Intercomparison and interpretation of climate feedback processes in 19 atmospheric general circulation models, *J. Geophys. Res.*, *95*, 16,601–16,615, 1990.

Dutton, J. A., An analytical model of atmospheric feedback and global temperature change, *J. Clim.*, *8*, 1122–1139, 1995.

Flohn, H., and A. Kapala, Changes in tropical sea-air interaction processes over a 30-year period, *Nature*, *338*, 244–245, 1989.

Gaffen, D. J., T. P. Barnett, and W. P. Elliott, Space and timescales of global tropospheric moisture, *J. Clim.*, *4*, 989–1008, 1991.

Hallberg, R., and A. K. Inamdar, Observation of seasonal variations of atmospheric greenhouse trapping and its enhancement at high sea surface temperature, *J. Clim.*, *6*, 920–931, 1993.

Hense, A., P. Krahe, and H. Flohn, Recent fluctuations of tropospheric temperature and water vapor content in the tropics, *Meteorol. Atmos. Phys.*, *38*, 215–227, 1988.

Inamdar, A. K., and V. Ramanathan, Physics of greenhouse effect and convection in warm oceans, *J. Clim.*, *5*, 715–731, 1994.

Intergovernmental Panel on Climate Change (IPCC), Scientific Assessment of Climate Change, 548 pp., World Meteorol. Organ./UNEP, Geneva, 1995.

Lau, K. M., C. H. Ho, and M. D. Chou, Water vapor and cloud feedback over the tropical oceans: Can we use ENSO as a surrogate for climate change?, *Geophys. Res. Lett.*, *23*, 2971–2974, 1996.

Lindzen, R. S., Some coolness concerning global warming, *Bull. Am. Meteorol. Soc.*, *71*, 288–299, 1990.

Lindzen, R. S., On the scientific basis for global warming scenarios, *Environ. Pollut.*, *83*, 125–134, 1994.

Lindzen, R. S., B. Kirtman, D. Kirk-Davidoff, and E. K. Schneider, Seasonal surrogate for climate, *J. Clim.*, *8*, 1681–1684, 1995.

Manabe, S., and R. T. Wetherald, Thermal equilibrium of the atmosphere with a given distribution of relative humidity, *J. Atmos. Sci.*, *24*, 241–259, 1967.

Mitchell, J. F. B., The "greenhouse effect" and climate change, *Rev. Geophys.*, *27*, 115–139, 1989.

Oort, A. H., and H. Liu, Upper air temperature trends over the globe, 1958–1989, *J. Clim.*, *6*, 292–307, 1993.

Ramanathan, V., The role of ocean-atmosphere interactions in the CO_2 climate problem, *J. Atmos. Sci.*, *38*, 918–930, 1981.

Ramanathan, V., R. D. Cess, E. F. Harrison, P. Minnis, B. R. Barkstrom, E. Ahmad, and D. Hartmann, Cloud-radiative forcing and climate: Results from the earth radiation budget experiment, *Science*, *243*, 57–63, 1989.

Ramanathan, V., and A. M. Vogelmann, Greenhouse effect, atmospheric solar absorption and the earth's radiation budget: From the Arrhenius-Langley era to the 1990s, *Ambio*, *26*, 38–46, 1997.

Ramanthan, V., and W. Collins, Thermodynamic regulation of ocean warming by cirrus clouds deduced from observations of the 1987 El Nino, *Nature*, *351*, 27–32, 1991.

Randel, D. L., T. H. Vonder Haar, M. A. Ringerud, G. L. Stephens, T. H. Greenwald, and C. L. Combs, A new global water vapor data set, *Bull. Am. Meteorol. Soc.*, *77*, 1233–1246, 1996.

Raval, A., and V. Ramanthan, Observational determination of the greenhouse effect, *Nature*, *342*, 758–761, 1989.

Reynolds, R. W., A real-time global sea surface temperature analysis, *J. Clim.*, *1*, 75–86, 1988.

Rind, D., E. W. Chiou, W. Chu, J. Larsen, S. Oltmans, J. Lerner, M. P. McCormick, and L. McMaster, Positive water vapor feedback in climate models confirmed by satellite data, *Nature*, *349*, 500–503, 1991.

Salisbury, J. W., and D. M. D'Aria, Emissivity of terrestrial materials in the 8–14 micron atmospheric window, *Remote Sens. Environ.*, *42*, 83–106, 1992.

Schroeder, S. R., and J. P. McGuire, Widespread tropical atmospheric drying from 1979 to 1995, *Geophys. Res. Lett.*, *25*, 1301–1304, 1998.

Schubert, S. D., J. Pjaendtner, and R. Rood, An assimilated data set for Earth science applications, *Bull. Am. Meteorol. Soc.*, *74*, 2331–2342, 1993.

Schubert, S., C.-K. Park, C.-Y. Wu, W. Higgins, Y. Kondratyeva, A.

Molod, L. Takacs, M. Seablom, and R. Rood, A multiyear assimilation with the GEOS-1 system, Overview and results, in Technical report series on global modeling and data assimilation, edited by M. J. Suarez, *NASA Tech. Memo. 104606*, vol. 6, 201 pp., 1995.

Soden, B. J., Variations in the tropical greenhouse effect during El Nino, *J. Clim., 10,* 1050–1055, 1997.

Soden, B. J., and R. Fu, A satellite analysis of deep convection, upper-tropospheric humidity, and the greenhouse effect, *J. Clim., 8,* 2333–2351, 1995.

Stephens, G. L., On the relationship between water vapor over the oceans and sea surface temperature, *J. Clim., 3,* 634–645, 1990.

Stephens, G. L., and T. J. Greenwald, The earth's radiation budget and its relation to atmospheric hydrology, 1, Observations of the clear sky greenhouse effect, *J. Geophys. Res., 96,* 15,311–15,324, 1991.

Waliser, D. E., N. E. Graham, and C. Gautier, Comparison of the highly reflective cloud and outgoing longwave radiation data sets for use in estimating tropical deep convection, *J. Clim., 6,* 331–353, 1993.

Wetherald, R. T., and S. Manabe, The effect of changing the solar constant on the climate of a general circulation model, *J. Atmos. Sci., 32,* 2044–2059, 1975.

Wielicki, B. A., R. D. Cess, M. D. King, D. A. Randall, and E. F. Harrison, Mission to planet earth: Role of clouds and radiation in climate, *Bull. Am. Meteorol. Soc., 76,* 2125–2153, 1995.

A. K. Inamdar and V. Ramanathan, Center for Clouds, Chemistry and Climate, DSDP A36, SIO, UCSD, Mail Code 0239, La Jolla, CA 92093. (e-mail: ainamdar@ucsd.edu)